

1 **Cu₂O Nano-flowers/Graphene Enabled Scaffolding Structure Catalyst Layer for**
2 **Enhanced CO₂ Electrochemical Reduction**

3 *Yucheng Wang¹, Hanhui Lei¹, Shun Lu, Ziming Yang, Ben Bin Xu, Lei Xing*, Terence Xiaoteng*
4 *Liu**
5

6 Dr. Yucheng Wang, Hanhui Lei, Prof. Ben Bin Xu, Dr. Terence Xiaoteng Liu
7 Faculty of Engineering and Environment, Northumbria University, Newcastle upon Tyne,
8 NE1 8ST, United Kingdom
9

10 Dr. Shun Lu
11 Department of Agricultural and Biosystems Engineering, South Dakota State University,
12 Brookings, SD 57007, USA
13

14 Dr. Ziming Yang, Dr. Lei Xing,
15 Department of Engineering Science, University of Oxford, Oxford OX1 3PJ, United Kingdom
16

17 ¹authors contributed equally to this work.

18

19

20

21

22

23

24

25

26

27

28 *To whom correspondence should be addressed:*

29 Dr. Terence Xiaoteng Liu: terence.liu@northumbria.ac.uk

30 Dr. Lei Xing: xinglei1314@gmail.com

31 **ABSTRACT:**

32 Nanosized Cu₂O catalysts with precisely controlled bud-to-blooming flower shapes are
33 synthesised using modified polyol method. The evolution of the shape when the catalysts are
34 applied to the gas diffusion electrodes improves the key factors influencing the catalyst layer,
35 e.g. volume porosity and triple-phase boundary contact areas. Numerical and experimental
36 studies revealed increased reactant molar concentration and improved CO₂ mass transfer due
37 to the structural changes, which influenced the electrochemical CO₂ reduction reaction
38 (eCO₂RR). The fully bloomed Cu₂O nanoflower catalyst, combined with the two-dimensional
39 (2D) structured graphene sheet, formed a catalyst layer with scaffolding structure that exhibited
40 the highest Faradaic efficiency (FE) of 93.20% towards CO at an applied potential of -1.0 V
41 vs. RHE in 1M KOH. These findings established the relationship between the catalyst layer
42 properties and mass transfer, based on which we could describe the effect of the structural
43 design of the catalyst layer on the eCO₂RR performance.

44 **Keywords:** *CO₂ reduction reaction, catalyst layer, nanoflower, graphene and modelling.*

45

46 1. INTRODUCTION

47 The 'net zero' target act has urged the development of carbon capture and utilisation
48 technologies, including direct carbon capture [1, 2], enhanced weathering [3, 4], photochemical
49 CO₂ conversion [5, 6] and electrochemical reduction [7, 8]. The electrochemical conversion of
50 carbon dioxide (CO₂) has attracted increasing research attention owing to its many advantages,
51 such as moderate reaction temperature, simple reaction setup, and high energy-density fuel
52 products (e.g. CO and formate), and is one of the most efficient methods for large-scale energy
53 storage, chemical production, and transportation systems [8, 9]. Moreover, electrochemical
54 CO₂ reduction reaction (eCO₂RR) is a controllable process, and different products can be
55 obtained by varying the catalyst architecture, electrolyte pH, applied potential, and electrolyser
56 design etc. [10]. The commercialisation of this technology depends on a high-performance,
57 stable catalyst. Significant effort has been made to overcome the challenges faced by catalysts,
58 such as low catalytic activity [11, 12], low selectivity [13, 14], and poor durability of the
59 reaction system [15, 16], which reduces the reaction efficiency. Inertness of CO₂ molecules
60 requires high activation potential [17-19], and the low solubility (~35 mM at 298 K, 1 atm) of
61 CO₂ in the electrolyte reduces the CO₂ mass transfer leading to hydrogen evolution reaction
62 (HER) [20-22].

63 Significant research has been done over the last few decades to design novel electrocatalysts
64 with enhanced Faradaic efficiency (FE) for a desired eCO₂RR product by controlling catalyst
65 element selection [7], surface morphology [23], particle size [24], crystallisation [25] and
66 architecture [26]. (1) The metallic catalysts for eCO₂RR with different elemental types afford
67 different products through different reaction routes [15]. The binding energy difference of the
68 *CO species in metallic electrocatalysts determines the selectivity of main products [27].
69 Although noble metals, such as Au, Ag, and Pt, exhibit better CO₂ selectivity toward CO than
70 other metallic catalysts under moderate overpotentials [28], their high cost prohibits their

71 commercialisation. Compared to noble metals, Cu has a low price and significant eCO₂RR
72 activity [8], and is the only metal that yields multiple products, such as CO, formate, methane,
73 ethane, ethylene, ethyne, methanol, ethanol and other C₂, or even C₃ organic products [29].
74 The selectivity of Cu-based catalysts depends on the catalyst morphology, local pH,
75 overpotential, and electrolyte concentration [9]. Therefore, the reaction conditions should be
76 carefully controlled to enhance the system selectivity. Cu oxide nanoparticles, such as cuprous
77 oxide (Cu₂O), have attracted significant attention owing to their relatively high reaction activity
78 for the conversion of CO₂ into CO, CH₄, or C₂ [30, 31] at relatively low applied potentials. (2)
79 The morphology of the catalyst can be tuned to enhance the catalytic reaction efficiency, with
80 specific morphological and electronic characteristics improving the selectivity and activity of
81 eCO₂RR. Hu et al.[32] reported a unique shape of bismuth-based nanosheets on flow-through
82 hollow fibre, with enhanced formate selectivity and activity, up to 85% with current density of

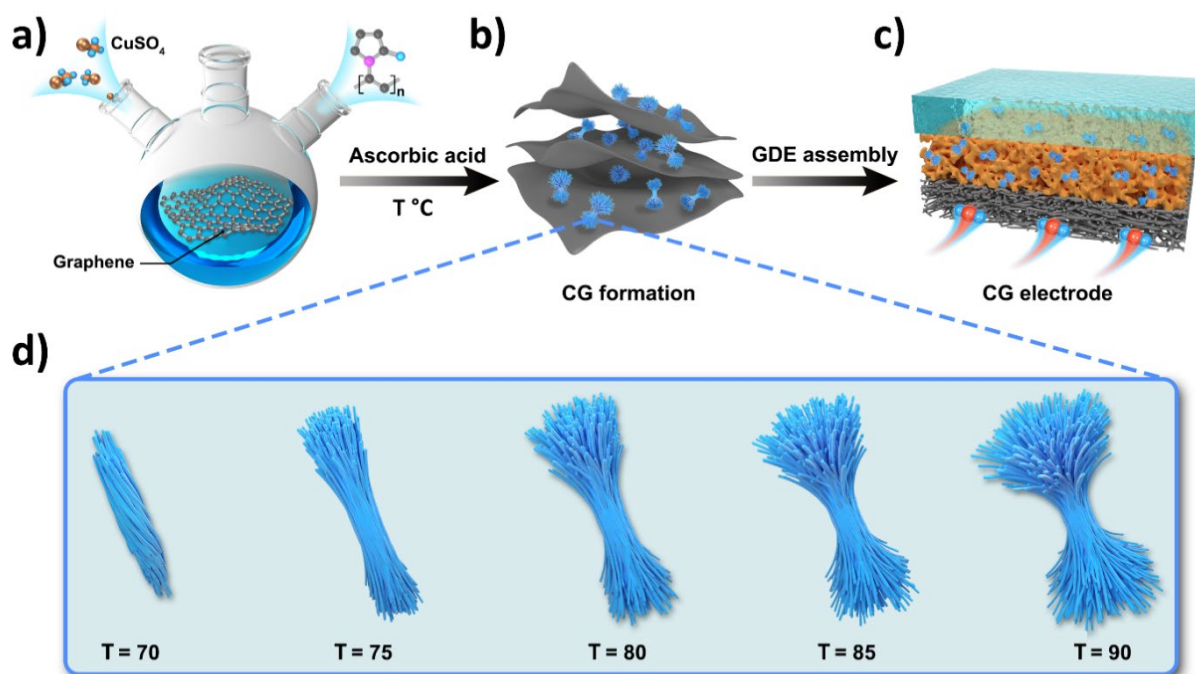


Figure 1 Scheme of CG electrodes for eCO₂RR. a) Modified polyol method for CG synthesis; b) CG formation on graphene layer; c) GDE assembly of CG electrode. d) Morphology of Cu₂O in CG by controlling the reaction temperature from 70 °C to 90 °C, where T (°C) represents the synthesis temperature.

83 141 mA cm⁻² at -1.0 V vs. RHE. Jiao et al.[33] developed a Pd octahedra catalyst, represents
84 up to 95% FE of CO and better reaction activity than Pd cubes.

85 The CO₂ mass transfer influences the efficiency of the reaction system. Recently, gas diffusion
86 electrode (GDE) cells have been employed [22, 34] for eCO₂RR, where CO₂ is fed directly
87 through the gas diffusion layer to the catalyst layer surface, with a short diffusion distance for
88 the gaseous reactants to reach the electroactive sites on the catalyst surface [35]. Wang et al.
89 [36] discovered a bilayer porous electrode with directional diffusion of gas molecules onto the
90 catalyst layer and 94% FE to carbonaceous products at -1.0 V vs. RHE and a current density
91 of 200 mA cm⁻². Dinh et al. [34] developed a polymer-based hydrophobic gas diffusion
92 electrode, which prevents flooding and has a stable catalyst surface on account of the carbon
93 nanoparticles and graphite, and exhibits 70% FE towards ethylene at -0.55 V vs. RHE.
94 Although the effects of the electrode structure and catalyst layer have been reported, the effects
95 of reduced mass transfer, porosity, and hydrophobicity of the catalyst-coated electrode on the
96 performance have not yet been studied.

97 A high-performance catalyst with considerable CO₂ mass transfer is required for an effective
98 reaction system. In this study, we synthesised a series of Cu₂O/graphene (CG) nanoflower
99 composite catalysts with precise bud-to-blooming flower opening degrees. The degree of
100 opening increases at each 5 °C along with temperature increase in synthesis temperature from
101 70 to 90 °C for each catalyst (**Figure 1**). The catalysts were printed on GDE as cathode catalyst
102 layers and assembled in a 3D-printed cell to study the effect of the induced mass transfer. The
103 fully bloomed nanoflower forms a scaffolding structure with the graphene sheets (Figure 1b),
104 and one such structure was assembled as the CG electrode. This resulted in a change in the
105 catalyst layer porosity (Figure 1c, orange middle layer), and the blooming flower petals
106 increased the exposure of Cu₂O active sites compared to the buds resulting in an improved
107 surface/volume ratio.

108 2. EXPERIMENTAL

109 2.1 Reagents

110 All the reagents were of analytical grade and were used without further purification. Copper
111 (II) sulfate pentahydrate ($\text{CuSO}_4 \cdot 5\text{H}_2\text{O}$, Sigma-Aldrich) was used as the copper precursor to
112 prepare the catalyst. Graphene powder was purchased from Goodfellow. Ethylene glycol
113 ($\text{C}_2\text{H}_6\text{O}_2$) was purchased from Fisher Scientific (U.K.). Polyvinylpyrrolidone (powder, wt.
114 10000) and L-ascorbic acid (powder) were purchased from Sigma Aldrich.

115 2.2 Catalyst Synthesis

116 The CG catalysts were synthesised using a modified polyol method. Initially, 53.5 mg of
117 graphene, 150 mg of L-ascorbic acid (99%, in 20 mL deionised water) solution, and 80 mL
118 ethylene glycol were mixed in a beaker and sonicated at 25 °C for 30 min to remove any oxide
119 formed on graphene. The suspension was transferred into a three-neck flask, and 200 mL of
120 ethylene glycol was added. Subsequently, polyvinylpyrrolidone (50 mg) was dissolved in 50
121 mL of deionised water and added to the flask. After that, 200 mg of $\text{CuSO}_4 \cdot 5\text{H}_2\text{O}$ (Cu:C = 1:1
122 (wt.%) was dissolved in 20 mL of deionised water and added to the flask dropwise. The
123 mixture was then stirred at 400 rpm for 10 h in N_2 atmosphere at 70 °C, 75 °C, 80 °C, 85 °C,
124 and 90 °C to obtain flower-like catalysts with different blooming degrees. The suspension was
125 then filtered and washed with ethanol to remove the residual chemicals. A brief schematic of
126 the synthesis procedure is illustrated in Figures 1 a, b, and d. Finally, the as-prepared catalysts
127 were dried in an open-air oven at 40 °C. The catalysts were annotated as CG1, CG2, CG3, CG4,
128 and CG5, corresponding to synthesis temperatures of 70, 75, 80, 85, and 90 °C, respectively.
129 We also synthesised a Cu_2O nanocube catalyst without graphene (which provides a dense
130 catalyst layer for eCO_2RR) to verify the effect of the catalyst layer structure using a previously
131 reported synthesis method [36].

132 2.3 Physical Characterisation

133 Scanning **electron** microscopy (SEM), combined with energy-dispersive X-ray spectroscopy
134 (EDX) (MIRA 3, TESCAN at an operating voltage of 10 kV), was used to study the
135 morphology and elemental distribution of the catalysts and electrodes. X-ray diffraction (XRD)
136 patterns were obtained on a Rigaku Smartlab II diffractometer with a nominal 3-kW X-ray
137 source to analyse the crystalline structure of the catalysts. An X-ray photoelectron spectroscope
138 (XPS) (SSX-100, Surface Science Laboratories, Inc.), equipped with a monochromatic
139 Al K α X-ray source, was used to characterise the catalyst surface. **The CGs were assembled**
140 **onto carbon paper for the XRD testing, and the CG powders for XPS analysis.**

141 2.4 Electrode Assembly

142 The catalyst powder (20 mg) was mixed with 1 mL ethanol in a 2-mL sample tube and
143 sonicated for 10 min. Nafion[®] solution (40 μ L; 5 wt.%, Sigma-Aldrich) was added to the tube
144 and sonicated for 1 h. The as-prepared ink was spray-painted onto carbon paper (H23C6,
145 Freudenberg) with an effective surface area of 2 cm². The process was repeated until the mass
146 increased (Δm) to 5 mg cm⁻². The catalysts on the gas diffusion layer (GDL) were characterised
147 using SEM/EDS.

148 2.5 Electrochemical Evaluation Methods

149 The electrochemical measurements were performed using an Autolab potentiostat/galvanostat
150 (Metrohm Autolab **PGSTAT302N**). Ag/AgCl and Pt wire were used as the reference and
151 counter electrodes, respectively. The reference electrode was converted to RHE using the
152 following equation:

$$153 \quad E_{RHE} = E_{Ag/AgCl} + 0.197 V + 0.0591 V \times pH \quad (1)$$

154 We studied the electrochemical performance of the catalysts for eCO₂RR using self-designed
155 GDE-cells, and the **full details of our** 3D printed device is shown in Figure S1 **in Supplementary**

156 **Information.** A carbon paper GDL served as the current collector and physical substrate for the
157 catalyst; Ag/AgCl and Pt wire were used as the reference and counter electrodes, respectively.
158 CO₂ gas was supplied using a gas inlet into the gas chamber and then diffused across the GDL
159 to reach the catalyst layer. The CO₂ gas flow rate was maintained at 15 mL min⁻¹ using a flow
160 meter (Cole-Parmer TMR1-010462). The influence of pH on the electrolyte was evaluated at
161 high pH (1 M and 5 M KOH as the catholyte and anolyte, respectively) and moderate pH (1 M
162 and 2 M KHCO₃ as the catholyte and anolyte, respectively). The electrolytes were pre-
163 electrolysed before the electrochemical test using chrono-potentiometry at a constant current
164 density of 3.5 mA cm⁻² using Pt-mesh electrodes for purification. The pre-purge of CO₂ is not
165 required in the electrolyte of the GDE cell. A cation exchange membrane (CEM, Fumapem F-
166 950) was placed between the catholyte and the anode, allowing the cations to transfer through
167 the membrane. The gas products were collected from the gas outlet, and the catholyte was
168 collected for liquid product analysis after the reaction.

169 To analyse eCO₂RR behaviour using different catalysts, we performed the chronoamperometry
170 (CA) tests at -0.4 V, -0.6 V, -0.8 V, -1.0 V and -1.2 V vs. RHE for 0.5 h, and measured the
171 current density (*j*) vs. the proceeding time (h). The FE of the electrochemical reaction can be
172 calculated using the input charge and processing time of the electrochemical process in CA,
173 along with the gaseous/liquid product measurement and molar mass calculation. The FEs of
174 the gaseous and liquid products were analysed after 4 h and 8 h of reaction.

175 **To investigate the catalysts' hydrogen evolution reaction (HER) reactivity for the purpose of**
176 **comprehensively understand the FE results, we performed the linear scanning voltammograms**
177 **(LSV) at the applied potential range from -0.1 V to -1.4 V vs. RHE at a scan rate of 50 mV s⁻¹**
178 **in 1 M KOH, with N₂ and CO₂ purged conditions, accordingly. The electric double layer**
179 **capacitance (C_{dl}) of catalysts were estimated by CV scans in the range of -0.1 V to 0.3 V vs.**

180 RHE in CO₂ saturated 1 M KOH, at the scan rates from 20 mV s⁻¹, 40 mV s⁻¹, 60 mV s⁻¹, 80
181 mV s⁻¹ and 100 mV s⁻¹ where no Faradaic reaction happens. The double layer capacitances
182 were calculated using the following equation[32, 37]:

$$183 \quad C_{dl} = J \left(\frac{dV}{dt} \right) \quad (2)$$

184 where J is the current density of 0.1 V vs. RHE, and $\frac{dV}{dt}$ is the scan rate of CVs.

185 To evaluate the stability of each catalyst, we performed CA tests in the GDE cell at an applied
186 potential of -1.0 V vs. RHE in 1 M KOH with a constant CO₂ gas supply (15 mL min⁻¹). The
187 long-term experiment was conducted for 8 h, and 100 mL catholyte was cycled throughout the
188 reaction.

189 **2.6 Products Analysis**

190 The gaseous products of eCO₂RR were collected from the outlet of the reaction cell and
191 analysed using gas chromatography (GC, Shimadzu Tracera GC-2010) coupled with a barrier
192 discharge ionisation detector (BID). The CO₂ flow rate was maintained at 15 mL min⁻¹ using a
193 flow meter.

194 The liquid product (formate) was collected from the catholyte and quantified using an ion
195 chromatography (Eco IC, Metrohm) equipped with a 'Metrohm 6.1005.200' column formic
196 acid identification. The FE value for each product was calculated according to Faraday's law
197 [8], and the detailed calculations are provided in the SI.

198 **2.7 COMSOL Simulation**

199 A multi-physics model based on COMSOL was implemented to investigate the mass transfer
200 and electrochemical reduction of CO₂ at a given flow rate, pressure, temperature, and potential.
201 The model consisted of an electrolyte chamber (EC), catalyst layer (CL), gas diffusion layer

202 (GDL), and gas chamber (GC) (Figure S2). The fluids through the chambers were assumed to
203 have a laminar flow, and the velocity profile in the porous electrode was described using the
204 Navier-Stokes equation. The calculated gas velocity was correlated with the convective mass
205 transport in the convection-diffusion-reaction equation. The Butler-Volmer equation was used
206 to correlate the relationship between current density and applied electrode potential, and
207 Faraday's law was applied to convert the current density to the generation/consumption rates
208 of chemical species in the system, which were used as the source/sink terms in the convection-
209 diffusion-reaction equation. The concentrations of various species, such as $\text{CO}_{2(\text{g})}$, $\text{CO}_{2(\text{aq})}$,
210 $\text{CO}_{(\text{g})}$, and formate, current and potential distributions, and velocity profiles were correlated,
211 and the hydrogen evolution reaction (HER) was considered as a side reaction. The detailed
212 model development is shown in Figure S2 and Table S1.

213 **2.8 Model Assumptions and Features**

214 The multi-physics model was developed based on the following assumptions:

- 215 • Reactant gas flowing through the cathode channels is treated as laminar flow.
- 216 • Sufficient CO_2 was supplied evenly at a constant flow rate at the cathode inlet, and the
217 ideal gas law was applied to the gas species.
- 218 • Temperature variation due to chemical reactions is neglected.
- 219 • Mass transport occurs through diffusive and convective mechanisms. The Soret effect
220 for mass transport was not considered because of the isothermal assumption.
- 221 • The pH of the bulk solution at the anode remained constant, and no acid-base equilibria
222 occurred at the catalyst layer-electrolyte boundary.
- 223 • Electrolyte conductivity is independent of the KOH concentration in the studied range.

224 The model considers the following processes: 1) the conservation of mass, species, charge, and
 225 momentum; 2) species transport through the porous electrode under diffusion and convection
 226 mechanisms; and 3) species generation and consumption inside the catalyst layer using
 227 electrical energy as the driving force. Additionally, the physical properties of the catalyst layer,
 228 such as thickness, pore size, and porosity, were also simulated for the catalyst morphology.
 229 The governing equations are given by Equations 3–10 and Equations S3–S11.

230 2.9 Governing Equations

231 The equations describing the conservation of momentum, mass, and species are discussed in
 232 the following section. Under the steady-state condition, the continuity equation is applied to
 233 describe the mass balance of the reactants flowing through the channel and porous electrode,
 234 leading to

$$\nabla \cdot (\rho_g u_g) = 0 \quad (3)$$

235 where ρ_g and u_g are the density and velocity, respectively, of the gas mixture.

236 For compressive Newtonian fluids, the Navier-Stokes equation is applied to simulate the
 237 variation in velocity and pressure within the channel, resulting in

$$\rho_g (u_g \cdot \nabla) u_g = \nabla \cdot \left[-PI + \mu_g (\nabla u_g + (u_g)^T) - \frac{2}{3} \mu_g (\nabla \cdot u_g) I \right] + \rho_g g \quad (4)$$

238 where P is the pressure, I is the identity matrix, μ_g is the dynamic viscosity of the gas mixture,
 239 and g is the gravitational acceleration. The above equation takes into account the effect of
 240 gravity on momentum balance.

241 The average diffusion model used in COMSOL was selected for species conservation in porous
 242 media and gas chambers, and the conservation of species is described by the following
 243 diffusion-convection-reaction equation:

$$\nabla \cdot N_i + (u_g \cdot \nabla)c_i = R_i \quad (5)$$

244 where N_i is the flux, c_i is the concentration, and R_i is the source/sink term of species i .

245 The above equation can be re-written as:

$$\nabla \cdot \left(-\rho_g D_{i,m} \nabla \omega_i - \rho_g \omega_i D_{i,m} \frac{\nabla M_g}{M_g} \right) + \nabla \cdot (\rho_g u_g \omega_i) = R_{i,m} \quad (6)$$

246 where ω_i is the mass fraction, M_g is the mean molar concentration of the gas mixture ($M_g =$
 247 $(\sum_j \frac{\omega_j}{M_j})^{-1}$), M_i is the molar concentration of species i , $D_{i,m}$ is the diffusivity of the gas mixture,
 248 which comes from the Maxwell-Stefan equation, and is calculated using $D_{i,m} = \frac{1-\omega_i}{\sum_{k \neq i} \frac{x_k}{D_{ik}}}$, x_k is
 249 the molar fraction of gas, and D_{ik} is the binary diffusivities of the species pairs.

250 The electrode reaction rate is controlled by charge transfer and is independent of mass transfer
 251 when the reactant supply is sufficient. The Tafel equation was chosen as the kinetic expression
 252 for the electrode, and the current density was obtained as follows:

$$i_{Ea} = -i_{o,Ea}^{ref} \left(\frac{C_{CO_2(aq)}}{C_{CO_2(aq),Ea}^{ref}} \right) \exp \left(-\frac{\beta_{Ea} F}{R_{ideal} T} (V_0 - V_1 - V_{eq,Ea}^{ref}) \right) \quad (7)$$

$$i_{Eb} = -i_{o,Eb}^{ref} \left(\frac{C_{CO_2(aq)}}{C_{CO_2(aq),Eb}^{ref}} \right) \exp \left(-\frac{\beta_{Eb} F}{R_{ideal} T} (V_0 - V_1 - V_{eq,Eb}^{ref}) \right) \quad (8)$$

$$i_{Ec} = -i_{o,Ec}^{ref} \exp\left(-\frac{\beta_{Ec}F}{R_{ideal}T}(V_0 - V_1 - V_{eq,Ec}^{ref})\right) \quad (9)$$

253 where $i_{o,Ej}^{ref}$ ($j = a, b, c$) are the reference exchange current densities for generating HCOO, CO,
 254 and H₂, respectively, $C_{CO_2(aq),Ea}^{ref}$ and $C_{CO_2(aq),Eb}^{ref}$ are the reference concentrations for producing
 255 HCOO and CO, respectively, R_{ideal} is the ideal gas coolant; β_{Ei} ($i = a, b, c$) are symmetry
 256 factors, F is the Faraday constant, and $V_{eq,Ei}^{ref}$ ($i = a, b, c$) are equilibrium potentials.

257 According to Faraday's law, the electrochemical reaction rates of CO₂, HCOO, CO, and H₂ can
 258 be obtained as follows:

$$R_{E,CO_2(aq)} = \frac{M_{CO_2} a_{sl} (i_{Ea} + i_{Eb})}{2F}; R_{E,HCOO} = -\frac{M_{HCOO} a_{sl} i_{Ea}}{2F};$$

$$R_{E,CO} = -\frac{M_{CO} a_{sl} i_{Eb}}{2F}; R_{E,H_2} = \frac{M_{H_2} a_{sl} i_{Ec}}{2F} \quad (10)$$

259 where M_{CO_2} , M_{HCOO} , M_{CO} , and M_{H_2} are the molecular weights of each species, a_{sl} is the
 260 specific area of the solid-liquid interface, and an idealised structure of the catalyst layer was
 261 designed to calculate the specific area a_{sl} . The details are presented in Figure S3. The other
 262 equations can be found elsewhere [38].

263 3. RESULTS AND DISCUSSION

264 3.1 Preparation and Characterisation of the Catalysts

265 The SEM morphology and EDS mapping spectra of the catalysts are shown in **Figure 2**. With
 266 an increase in temperature from 70 °C to 90 °C, the opening degree of the petals increased
 267 gradually; it started with nanobuds at 70 °C and developed into nanoflowers at 90 °C. The
 268 longitudinal length of CGs range between 1.3 μm and 1.7 μm, and the diameter of each petal
 269 is 40 nm. For comparison, the Cu₂O nanoparticle was characterised (Figure S4a), and they
 270 demonstrated a cubic shape with an average particle size of 100 nm. The EDS mappings of
 271 CGs1–5 were studied for elemental analysis (Figures 2 f–o) and indicated an even distribution
 272 of Cu and O throughout the nanoparticles.

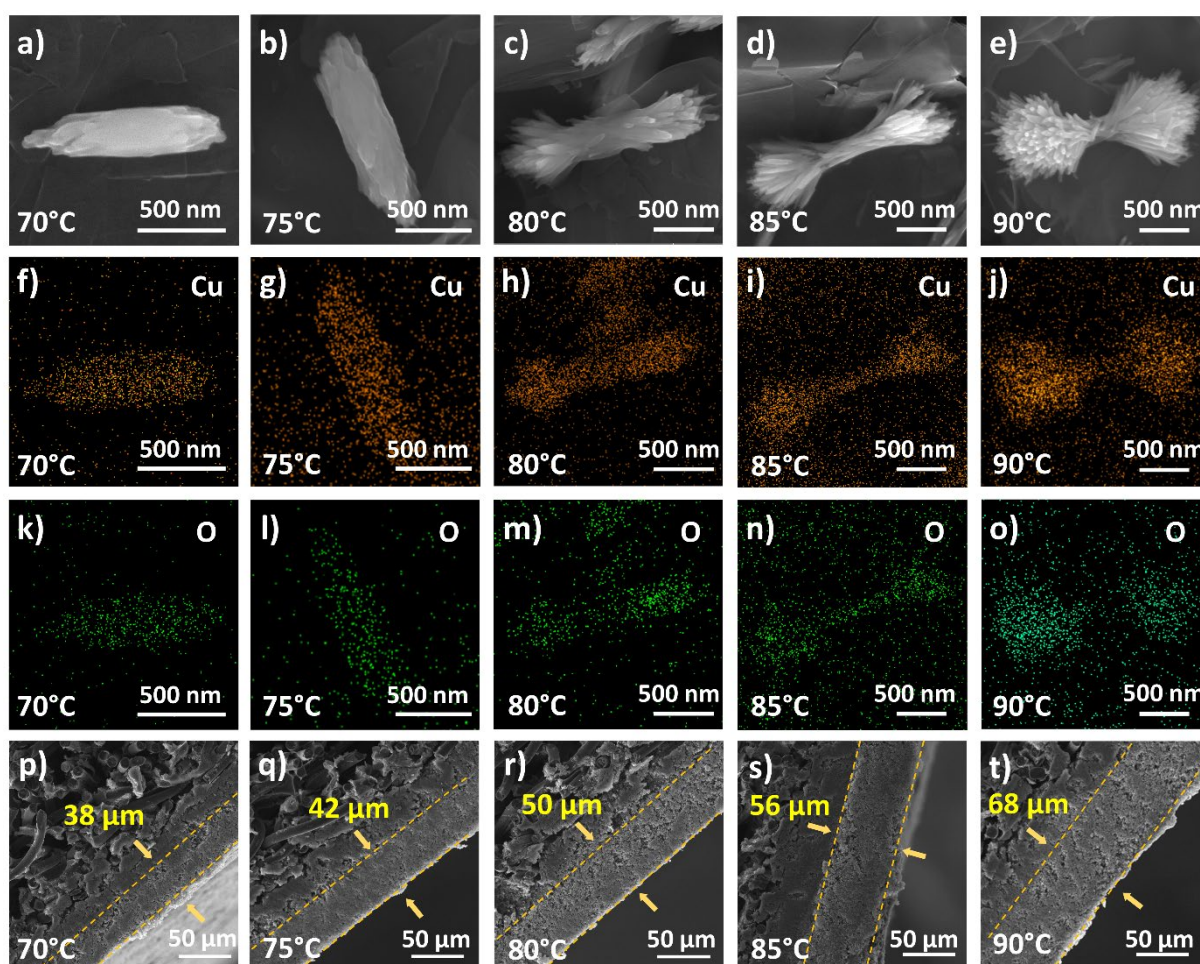


Figure 2 SEM scanning of a–e) Cu₂O nanoparticles on CG1–5 catalysts; EDS mapping of the composition of samples CG1–5; f–j) Cu and k–o) O elemental distribution; p–t) Thickness of catalyst layer via cross-section view of CGs1–5 assembled electrode.

273 SEM was used to study the cross-sectional morphology of all the gas diffusion electrodes to
 274 calculate the thickness of each CG catalyst layer (Figures 2 p–t). The electrodes were
 275 assembled with the same catalyst weight loading and coating area. The thickness of the CG
 276 catalysts increased with increasing degree of flower opening, indicating a reduction in the
 277 density and increase in the porosity of the catalyst layer with increasing thickness. The catalyst
 278 layer of the CGs exhibited a 'sponge' layer rather than a 'compressed layer', and the average
 279 thicknesses of CGs1–5 were 38 μm , 42 μm , 50 μm , 56 μm , and 68 μm , respectively. The
 280 catalyst layer thickness for the cubic Cu_2O catalyst was 18 μm (Figure S4b).

281 The crystal structure and atomic structure of the CG catalysts were analysed using XRD and
 282 XPS (**Figure 3**). The XRD pattern of all CG catalysts (Figure 3a) shows identical characteristic
 283 diffraction peaks of Cu_2O at $2\theta = 30^\circ, 36^\circ, 42^\circ, 61^\circ, 74^\circ,$ and 78° , corresponding to (110),

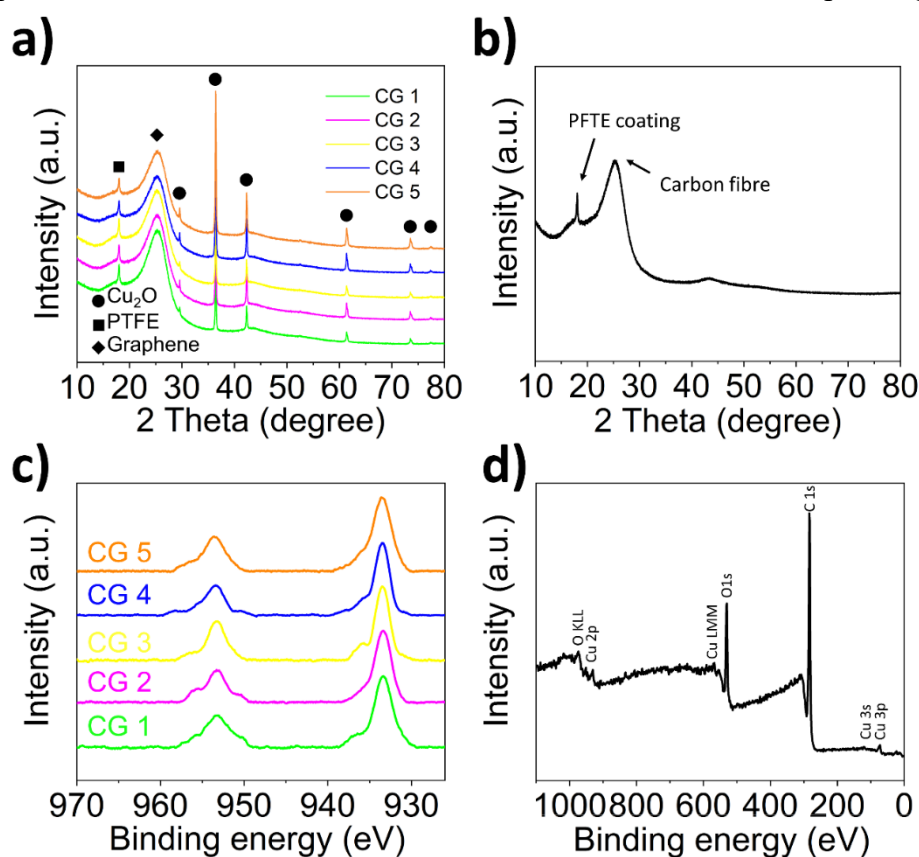


Figure 3 XRD patterns of a) CG electrodes, b) PTFE coated carbon paper as gas diffusion layer, c) XPS spectra of Cu 2p regions of CG catalysts and d) XPS survey spectrum of CG catalysts

284 (111), (200), (220), (311), and (222) planes, respectively; the peak at $2\theta = 18^\circ$ indicates the
285 PTFE coating on carbon paper (Figure 3b), while the broad peak at $2\theta = 25^\circ$ corresponds to
286 graphene. In our experiments, the crystallinity of the catalysts did not influence the CG
287 catalysts performance themselves. To further prove this observation, the average crystallite size
288 was calculated using XRD and shown in Table S2, where all CG catalysts present similar
289 average crystallite size of ca. 31 nm. The XPS Cu 2p spectra of CGs 1–5 are shown in Figure
290 3c, where the Cu-related peaks are symmetric. The absence of satellite structure at 943 eV rules
291 out Cu^{2+} in the CG catalysts [39]. The two apparent peaks at 933 eV and 953 eV are attributed
292 to the $\text{Cu}2p_{3/2}$ and $\text{Cu}2p_{1/2}$ peaks, respectively, of the Cu^+ in Cu_2O . The XPS results were
293 consistent for all the catalysts. The XPS survey spectra of CGs 1–5 present a similar pattern
294 (Figure 3d), confirming the presence of copper, oxygen, and carbon species. The XRD and
295 XPS results confirmed the similar crystal and atomic structure of these five CG catalysts,
296 indicating that the effect on eCO_2RR performance of CG1–CG5 depends purely on the catalyst
297 morphology-induced catalyst layer property variations.

298 **3.2 COMSOL Simulation of Catalyst Layer for eCO_2RR**

299 The effect of different catalyst layers was simulated to study the properties of CG catalysts for
300 eCO_2RR and to analyse the mass transfer and conversion of CO_2 gas within the cells. The CO_2
301 molar concentrations in the gas chamber and the gas velocity inside the catalyst layers were
302 investigated mathematically using the model developed in COMSOL Multiphysics[®].

303 We calculated the specific interfacial area of each CG catalyst layer, which corresponds to the
304 porosity of each CG catalyst. The pore sizes of the CG catalysts (29, 32, 35, 37, and 40 μm
305 corresponding to CGs1–5, respectively) were calculated using Equations S7 and S8 (Figure
306 4a). The specific interfacial area exhibited a strong linear relationship with the pore radius. The
307 slope of the linear fitting of the solid-liquid (catalyst layer-electrolyte) interface indicates a

308 minor influence of the pore size of the catalyst layer on the solid-liquid interface. The gas-
 309 liquid (CO₂-electrolyte) interface improves with increasing pore size, resulting in enhanced

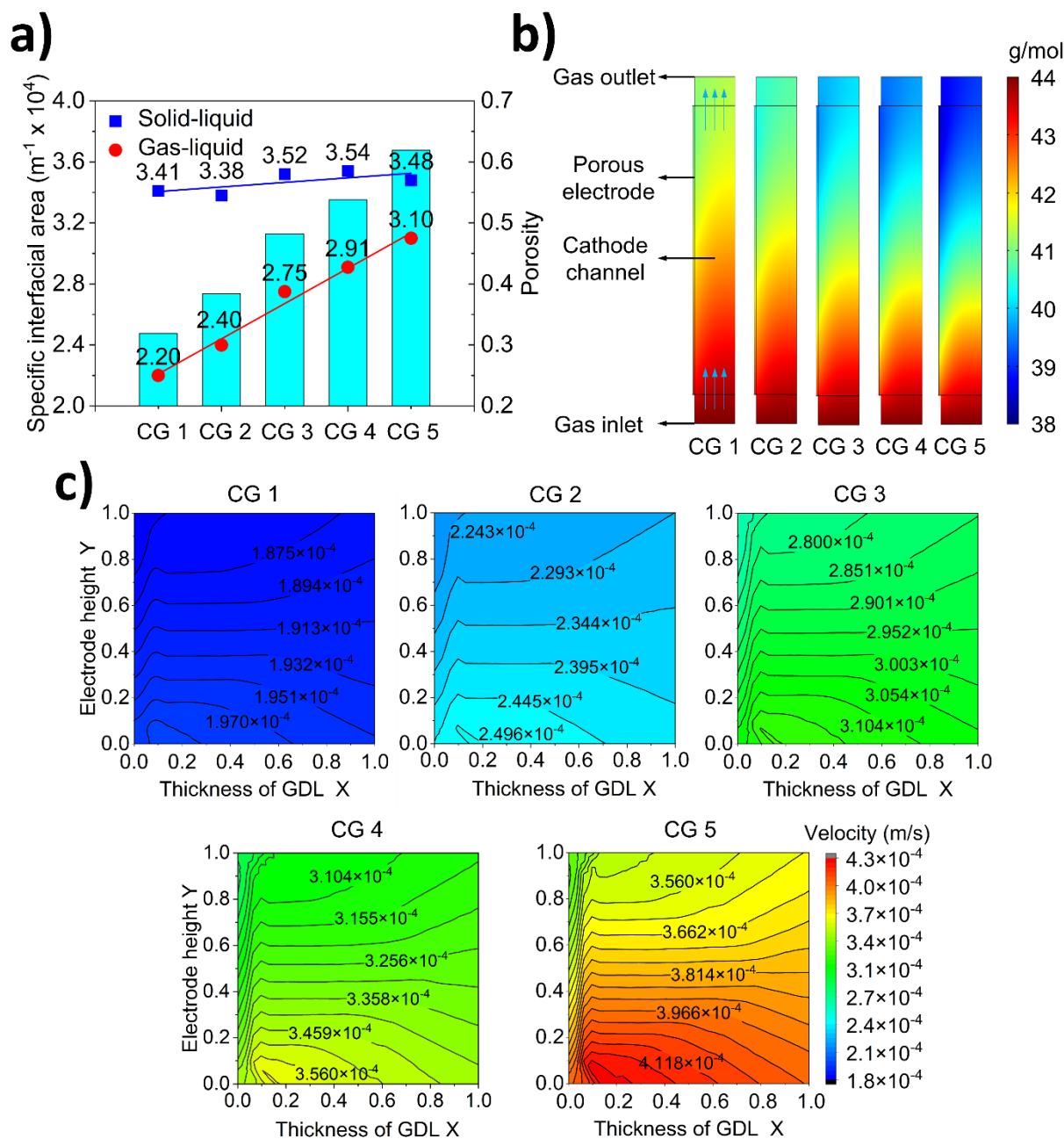


Figure 4 a) Specific interfacial area of CG catalysts layer (line-plot correspond to specific interfacial area, and the column plot correspond to porosity). b) Mean molar mass in CG, GDL, CL at -1.0 V vs. RHE, where the upper and bottom boxes represent the outlet and inlet of the gas chamber, the cylinder in the middle is the gas chamber. The thin layer attached to GDL on the left side is CL which has different parameters. c) Average CO₂ gas flow velocity in GDL at -1.0 V vs. RHE, where X = 0 for the 'CL-GDL' interface, X = 1 for the 'GDL-gas chamber' interface. Y = 0 for cathode inlet, Y = 1 for cathode outlet.

310 mass transfer rate of CO₂ from the gaseous to aqueous phase owing to the increased contact
311 area between CO₂ and the electrolyte.

312 Figure 4b shows the CO₂ mass concentration within the GDE cell, and the CO₂ concentration
313 declines across the top half of the chambers from CG1 to CG5. The CG5 catalyst exhibited the
314 lowest CO₂ concentration near the outlet of the gas chamber, indicating the highest CO₂
315 consumption in CG5. Therefore, CG5 demonstrates the highest mass transfer and reaction
316 efficiency and FE toward CO. The CO₂ gas velocity in the GDE cell at an applied potential of
317 -1.0 V vs. RHE, corresponding to eCO₂RR, is shown in Figures 4c. $X = 0$ indicates the
318 interface between the carbon paper/GDL and catalyst layer, and $X = 1$ corresponds to the
319 interface between the catalyst layer and gas chamber. $Y = 0$ and $Y = 1$ represent the boundaries
320 of the GDL near the gas inlet and outlet, respectively. CG5 exhibited the highest velocity within
321 the GDL on account of its **highest** porosity. The velocity peaks near $X = 0.1$ correspond to the
322 partial blockage of the CO₂ flow due to CL, resulting in velocity loss. The higher velocity near
323 the gas inlet compared to the gas outlet can be attributed to the **loss of gas fluid momentum**
324 **owing to the CO₂ captured inside the porous electrode, including GDL and CL. The simulation**
325 **results indicated a linear correlation between the nanoflower opening degree and the porosity**
326 **and surface/volume ratio.** The improved gas velocity indicated enhanced mass transport via a
327 convective mechanism, which accelerated the dissolution of gaseous CO₂ into the electrolyte
328 and increased the concentration of aqueous CO₂ resulting in fast eCO₂RR kinetics. The
329 increased specific area changes the internal structure of the catalyst layer by creating more
330 pores that trap the reactant gas (CO₂) within the catalyst layer, forming a robust gas-liquid-
331 solid interface for eCO₂RR. Additionally, the porous catalyst also mitigates the GDL
332 flooding[40]. The results indicate higher CO₂ absorption and higher CO₂ velocity within the
333 catalyst layer due to the increased specific area **and porosity**, which improve the CO₂ reaction
334 and mass transport activity.

335 3.3 Electrochemical CO₂ Reduction Reaction of CG Catalysts in GDE Cell

336 The eCO₂RR properties of all the CG catalysts were evaluated using a GDE cell reaction
337 system, and the FE results of the CG catalysts and Cu₂O cubic nanoparticles in 1 M KOH are
338 shown in **Figure 5**. The total current density and CO partial current density are shown in **Figure**
339 **6**, and the detailed data with error analysis are available in **Tables S3–S10**. The lower FEs for
340 CO in the bud-shaped CG1 catalyst correspond to 56.53%, 59.23%, 63.91%, 68.97% and
341 67.18% at -0.4 V, -0.6 V, -0.8 V, -1.0 V, and -1.2 V vs. RHE, respectively. CG1 also exhibits
342 the lowest current density due to the reduced surface area/volume ratio, which reduces the
343 number of active sites on the surface. The FE and current density of carbonaceous products
344 increase from CG1 to CG5 because of the increase in active sites on the catalyst surface and
345 enhanced porosity of the catalyst layer, which promote the reaction activity and CO₂ mass
346 transfer. The increased porosity of CG5 resulted in increased surface area of the solid-liquid
347 and gas-liquid interfaces and enhanced the reaction. The FEs at -0.4 V, -0.6 V, -0.8 V, -1.0
348 V, and -1.2 V vs. RHE are 74.43%, 79.84%, 87.26%, 93.20%, and 91.14%, respectively. The

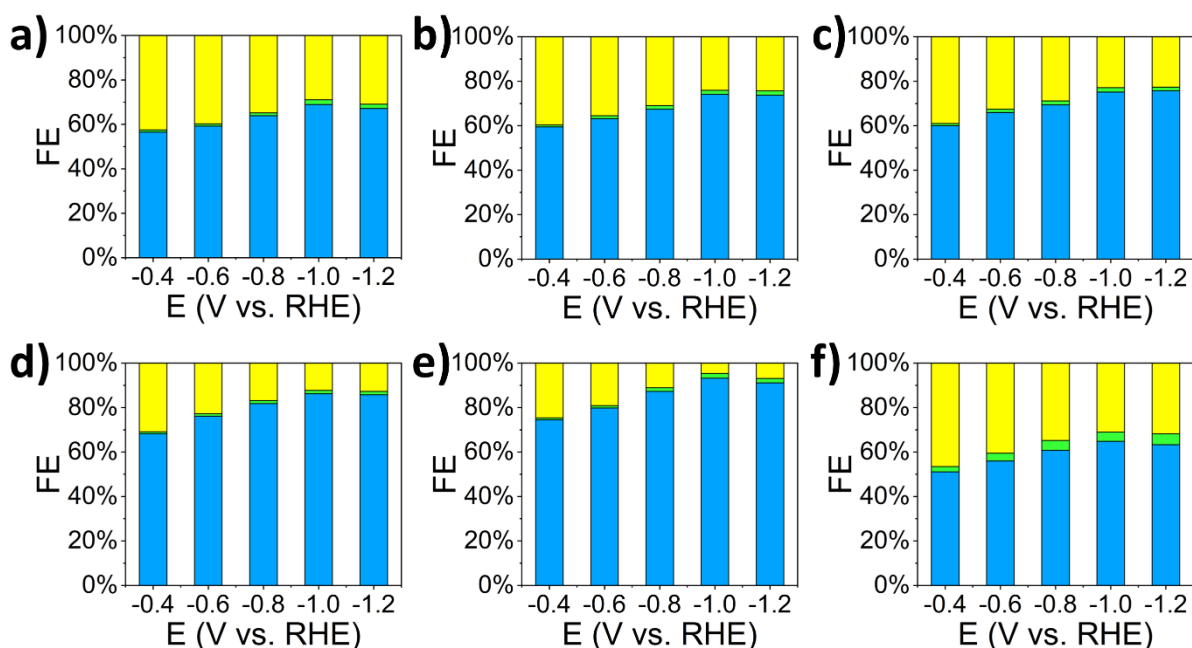


Figure 5 Faradaic efficiency profiles of a–e) CGs1–5 and f) Cu₂O in 1 M KOH electrolyte for eCO₂RR with products including CO (blue), formate (green), and H₂ (yellow)

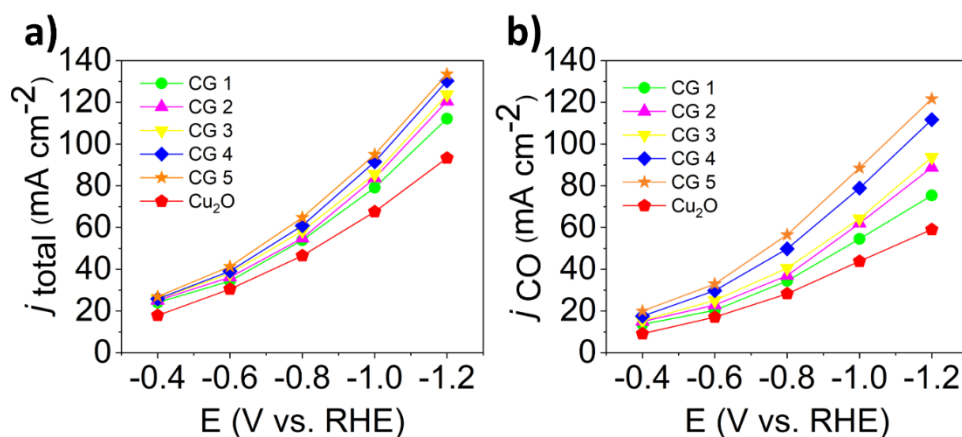


Figure 6 a) Total current density and b) current density of CO for CGs1–5 and Cu₂O in 1 M KOH electrolyte.

349 Cu₂O exhibited lower activity and selectivity toward eCO₂RR compared to the CG catalysts.
 350 The graphene in the CG catalysts separate the Cu₂O and provides a better gas-liquid-solid
 351 interface, thereby promoting charge transfer and CO₂ mass transfer within the catalyst layer.
 352 Contrastingly, pure Cu₂O (Figure 5f) does not form a porous structure within the catalyst layers,
 353 which reduces the CO₂ mass transfer and promotes the HER, resulting in poor eCO₂RR [36].
 354 The FEs at -0.4 V, -0.6 V, -0.8 V, -1.0 V, and -1.2 V vs. RHE are 51.07%, 55.98%, 60.80%,
 355 64.85% and 63.31%, respectively. Additionally, the crystal structures also affect the
 356 composition of gaseous and liquid products.

357 To further investigate the performance of CG catalysts in eCO₂RR, we performed LSV for all
 358 CG catalysts and Cu₂O. The results are shown in Figure S5a. In N₂-fed condition, all catalysts
 359 present a trend of lower current densities at less negative potentials, and gradually increased at
 360 higher potentials contributed by HER. While in CO₂-fed condition, the current density
 361 increases sharply at higher potentials where CO₂RR happens and suppresses the HER. The CG5
 362 presents the highest reaction activity, which agrees well with FE measurement. The statements
 363 were confirmed by measuring the double-layer capacitances (C_{dl}) under different scanning
 364 rates. As shown in Figure S5b, the C_{dl} of CGs increases from CG1 to CG5, by enhancing their

365 internal porosity, and the C_{dl} of CG5 presents over 6 times than that of Cu_2O . It is believed that
366 the presence of graphene allows the nanoflower evenly distributed on the surface and avoid the
367 agglomeration which enhanced its surface active sites. Figure S5c shows the Tafel parameters
368 of different CGs and Cu_2O for eCO_2RR . All Tafel slopes are lower than 118 mV dec^{-1} , which
369 suggests the same mechanism for CO_2 reduction reaction[32]. With increased porosity and
370 changed morphology of the catalysts, the Tafel plots were decreased from 82.1 mV dec^{-1} to
371 70.7 mV dec^{-1} , indicating faster kinetics and higher activity of eCO_2RR .

372 Above results indicate the synergistic effect between the Cu_2O nanoflower and graphene sheets
373 on the catalyst layer enhances the conversion of CO_2 to carbonaceous products. Initially, the
374 CG catalyst forms a porous layered structure that enhances the CO_2 retention and CO_2 mass
375 transfer. Additionally, the porous catalyst layer enhances the internal hydrophobicity and
376 prevents electrode flooding by electrolyte. The Cu_2O -graphene interaction changes the
377 electronic structure [41], and the Cu_2O particles prevent the HER in graphene, resulting in a
378 2D surface sufficient for Cu_2O to distribute and enhance the surface area of the proton-enriched
379 electrode. The combined effects of these factors yield improved eCO_2RR results.

380 The eCO_2RR was performed at moderate pH to study the effect of electrolyte alkalinity in
381 aqueous electrochemical CO_2 reduction using CG catalysts (Figure S6). Within the potential
382 range from -0.4 V to -1.2 V vs. RHE, the FE and current density of carbonaceous products
383 increase from CG1 to CG5, aligning well with the 1 M KOH electrolyte results. The CG5 with
384 nanoflower-shaped structure (Figure S6e) exhibits the FE of 53.11%, 63.90%, 70.12%, 72.72%
385 and 71.82% at -0.4 V , -0.6 V , -0.8 V , -1.0 V , and -1.2 V vs. RHE, respectively. The FEs of
386 Cu_2O (Figure S6f) at potentials of -0.4 V , -0.6 V , -0.8 V , -1.0 V , and -1.2 V vs. RHE are
387 21.56%, 34.31%, 47.87%, 52.90% and 54.71%, respectively.

388 Owing to the increase in surface area and porosity, the FE and current density of the
 389 carbonaceous products increases from CG2 through CG3 to CG4 (Figures S6 b–d). The current
 390 density and FE of carbonaceous products for 1 M KHCO₃ were lower than 1 M KOH. The
 391 strong base electrode suppresses HER and promotes eCO₂RR [22]. The results in 1 M KHCO₃
 392 confirm that the eCO₂RR can be enhanced using catalysts with higher active sites and a porous
 393 structure. The detailed data and relevant random errors are listed in **Tables S11–S18**. The
 394 simulation can be applied to any reaction regardless of the electrolyte.

395 3.4 Stability Evaluation of CG Catalysts in GDE Cell

396 The stability of the eCO₂RR reaction system is essential for commercial implementation
 397 because the GDLs may lose their hydrophobicity and permeate by electrolyte after a long-term

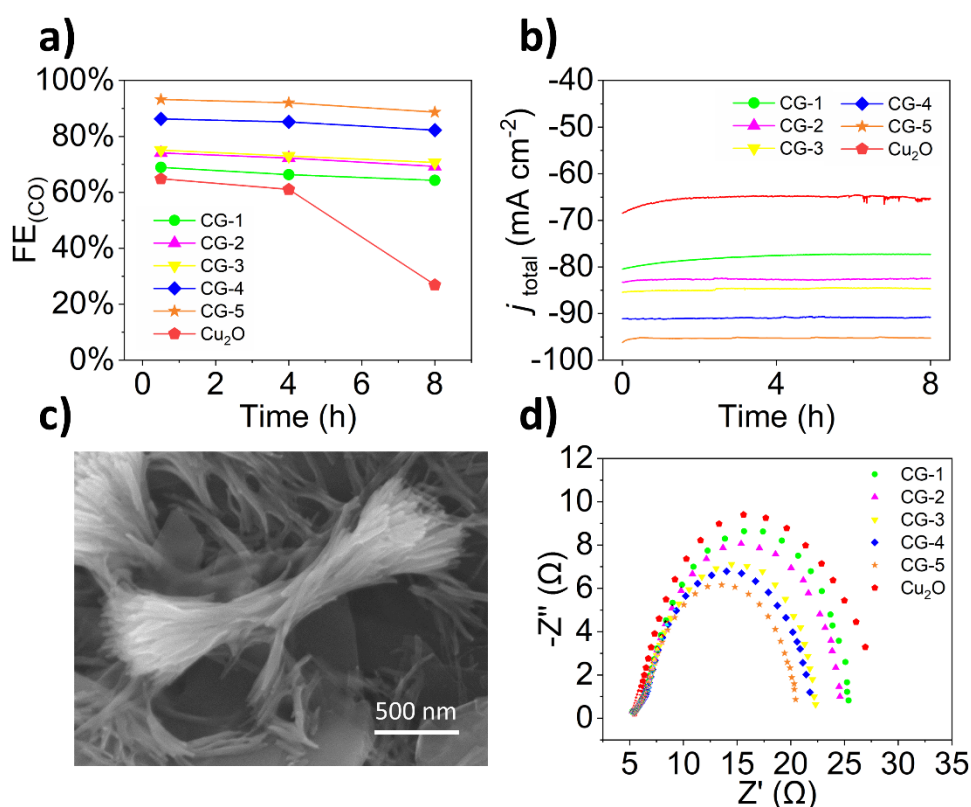


Figure 7 a) FE_{CO} results of stability test after 0.5 h, 4 h, and 8 h reaction of the CG catalysts at -1.0 V vs. RHE. b) Stability tests of CGs1–5 and Cu₂O at -1.0 V vs. RHE for 8 h in 1 M KOH, GDE system. c) SEM image of CG5 after 8 h reaction. d) Electrochemical impedance spectroscopy of CG catalysts and Cu₂O in 1 M KOH.

398 reaction [42]. The CG catalysts retain good FE of CO (**Figure 7**) after the 4-h and 8-h tests
399 compared to the half-hour reaction (Figure 7a, detailed data and relevant random error are listed
400 in **Tables S19 and S20**). The current remains stable after 8 h, and the FE values of CO for
401 CGs1–5 after 8 h of reaction were 64.30%, 69.26%, 70.69%, 82.23%, and 88.69%, respectively.
402 The hydrophobic porous CG catalyst layer prevents electrolyte penetration during the reaction.
403 The increase in thickness of the hydrophobic layer from CGs1–5 reduces the electrolyte
404 permeation through the GDL. The enhanced porosity of the catalyst layer increases the gas-
405 liquid-solid (CO₂-electrolyte-catalyst) interface, which enhances the active sites for eCO₂RR.
406 Conversely, the FEs decreased significantly after 8 h of reaction using Cu₂O, and the
407 corresponding FE of CO is 26.91%. Additionally, the CA plot becomes unstable due to
408 electrode permeation. To further explore the reason for the stability of the CG catalysts, we
409 scanned the CG5 electrodes using SEM after the reaction (Figure 7c). The CG retains the
410 nanoflower shape, even though the outer layers fall on the graphene sheets. Therefore, the
411 catalyst retains a high surface area for the reaction. Cu₂O nanoparticles exhibited a reduced FE
412 due to the damage of the catalyst surface (Figure S7) owing to the electrochemical corrosion,
413 which reduces the number of active sites on its surface and reduces the eCO₂RR performance.
414 Impedance spectroscopy was performed on CG catalysts and Cu₂O cubic catalyst at 0.1 V vs.
415 RHE to study the charge transfer of the CG catalysts (Figure 7d). The Nyquist plots indicate
416 an increasing trend for all the CG catalysts with the blooming process. The increase in porosity
417 of the catalysts improves the internal charge transfer, which results in enhanced eCO₂RR
418 performance. In contrast, the Cu₂O exhibited higher internal resistance, leading to a lower
419 current density for the eCO₂RR.

420 **4. CONCLUSIONS**

421 We developed an architecture-controlled catalyst for the electrochemical conversion of CO₂ to
422 CO. The temperature-dependent CG catalysts with controllable morphologies enhance the

423 eCO₂RR activity and efficiency by enhancing the gas-liquid and liquid-solid specific areas and
424 the porosity of the catalyst layer. Increasing the concentration of the incoming CO₂ near the
425 catalyst layer surface increased the CO₂ concentration within the catalyst layer and enhanced
426 the CO₂ velocity in the gas chamber, thereby improving the eCO₂RR. The enhanced
427 hydrophobicity of the catalyst layer provided considerable stability to the eCO₂RR system. FE
428 higher than 90% for CO and formate was obtained for CG5 catalyst at -1.0 V vs. RHE in a 1
429 M KOH electrolyte. The highly porous catalyst layer is hydrophobic and prevents the GDL
430 from being flooded, thereby enhancing the stability with a low FE drop after 8 h of reaction.
431 The enhanced conductivity and active sites of CG5 promote the reaction activity at a current
432 density of 133.5 mA cm⁻² and applied potential of -1.2 V vs. RHE.

433 Although the catalyst did not form the desired nano-bud or nanoflower structure at
434 temperatures below 70 °C and above 90 °C from the experimental aspect, this study has
435 established a theoretical analysis of the relationship between the CL intensity/mass transfer and
436 the induced eCO₂RR performance.

437

438 **ACKNOWLEDGMENTS**

439 This work was supported by the UK Engineering Physics and Science Research Council (Grant
440 No. EP/S032886/1), and the Royal Society International Exchanges Award (Grant No.
441 IEC\NSFC\201008)

442 **SUPPORTING INFORMATION**

443 Supporting Information is available from xxx.

444 **DECLARATION OF INTERESTS**

445 There are no conflicts to declare.

446 **REFERENCES**

- 447 [1] T. Wilberforce, A. Olabi, E.T. Sayed, K. Elsaid, M.A. Abdelkareem, Progress in carbon
448 capture technologies, *Science of The Total Environment*, (2020) 143203.
449 [2] A.I. Osman, M. Hefny, M. Abdel Maksoud, A.M. Elgarahy, D.W. Rooney, Recent
450 advances in carbon capture storage and utilisation technologies: a review, *Environmental*
451 *Chemistry Letters*, 19 (2021) 797-849.
452 [3] P. Renforth, The negative emission potential of alkaline materials, *Nature communications*,
453 10 (2019) 1-8.
454 [4] L. Xing, R.C. Darton, A. Yang, Enhanced weathering to capture atmospheric carbon
455 dioxide: Modeling of a trickle-bed reactor, *AIChE Journal*, 67 (2021) e17202.
456 [5] J. Fu, K. Jiang, X. Qiu, J. Yu, M. Liu, Product selectivity of photocatalytic CO₂ reduction
457 reactions, *Materials Today*, 32 (2020) 222-243.
458 [6] G. Zhao, X. Huang, X. Wang, X. Wang, Progress in catalyst exploration for heterogeneous
459 CO₂ reduction and utilization: a critical review, *Journal of Materials Chemistry A*, 5 (2017)
460 21625-21649.
461 [7] J. Qiao, Y. Liu, F. Hong, J. Zhang, A review of catalysts for the electroreduction of carbon
462 dioxide to produce low-carbon fuels, *Chem Soc Rev*, 43 (2014) 631-675.
463 [8] D.D. Zhu, J.L. Liu, S.Z. Qiao, Recent advances in inorganic heterogeneous electrocatalysts
464 for reduction of carbon dioxide, *Advanced materials*, 28 (2016) 3423-3452.
465 [9] Y. Zheng, A. Vasileff, X. Zhou, Y. Jiao, M. Jaroniec, S.-Z. Qiao, Understanding the
466 roadmap for electrochemical reduction of CO₂ to multi-carbon oxygenates and hydrocarbons
467 on copper-based catalysts, *Journal of the American Chemical Society*, 141 (2019) 7646-7659.
468 [10] S. Liang, N. Altaf, L. Huang, Y. Gao, Q. Wang, Electrolytic cell design for
469 electrochemical CO₂ reduction, *Journal of CO₂ Utilization*, 35 (2020) 90-105.
470 [11] D.C. Grills, Y. Matsubara, Y. Kuwahara, S.R. Golisz, D.A. Kurtz, B.A. Mello,
471 Electrochemical CO₂ Reduction with a Homogeneous Catalyst in Ionic Liquid: High Catalytic
472 Activity at Low Overpotential, *J Phys Chem Lett*, 5 (2014) 2033-2038.
473 [12] H.A. Hansen, J.B. Varley, A.A. Peterson, J.K. Nørskov, Understanding Trends in the
474 Electrochemical Activity of Metals and Enzymes for CO₂ Reduction to CO, *J Phys Chem Lett*,
475 4 (2013) 388-392.
476 [13] S. Nitopi, E. Bertheussen, S.B. Scott, X. Liu, A.K. Engstfeld, S. Horch, B. Seger, I.E.
477 Stephens, K. Chan, C. Hahn, Progress and perspectives of electrochemical CO₂ reduction on
478 copper in aqueous electrolyte, *Chemical reviews*, 119 (2019) 7610-7672.

479 [14] T. Hatsukade, K.P. Kuhl, E.R. Cave, D.N. Abram, T.F. Jaramillo, Insights into the
480 electrocatalytic reduction of CO₂ on metallic silver surfaces, *Phys Chem Chem Phys*, 16
481 (2014) 13814-13819.

482 [15] W. Zhang, Y. Hu, L. Ma, G. Zhu, Y. Wang, X. Xue, R. Chen, S. Yang, Z. Jin, Progress
483 and Perspective of Electrocatalytic CO₂ Reduction for Renewable Carbonaceous Fuels and
484 Chemicals, *Adv Sci (Weinh)*, 5 (2018) 1700275.

485 [16] R. Francke, B. Schille, M. Roemelt, Homogeneously Catalyzed Electroreduction of
486 Carbon Dioxide-Methods, Mechanisms, and Catalysts, *Chem Rev*, 118 (2018) 4631-4701.

487 [17] C.-H. Huang, C.-S. Tan, A review: CO₂ utilization, *Aerosol and Air Quality Research*, 14
488 (2013) 480-499.

489 [18] X. Xiaoding, J. Moulijn, Mitigation of CO₂ by chemical conversion: plausible chemical
490 reactions and promising products, *Energy & Fuels*, 10 (1996) 305-325.

491 [19] C.M. Gabardo, C.P. O'Brien, J.P. Edwards, C. McCallum, Y. Xu, C.-T. Dinh, J. Li, E.H.
492 Sargent, D. Sinton, Continuous carbon dioxide electroreduction to concentrated multi-carbon
493 products using a membrane electrode assembly, *Joule*, 3 (2019) 2777-2791.

494 [20] J. Durst, A. Rudnev, A. Dutta, Y. Fu, J. Herranz, V. Kaliginedi, A. Kuzume, A.A.
495 Permyakova, Y. Paratcha, P. Broekmann, Electrochemical CO₂ reduction—a critical view on
496 fundamentals, materials and applications, *CHIMIA International Journal for Chemistry*, 69
497 (2015) 769-776.

498 [21] T. Zheng, K. Jiang, N. Ta, Y. Hu, J. Zeng, J. Liu, H. Wang, Large-scale and highly
499 selective CO₂ electrocatalytic reduction on nickel single-atom catalyst, *Joule*, 3 (2019) 265-
500 278.

501 [22] H. Xiang, S. Rasul, K. Scott, J. Portoles, P. Cumpson, H.Y. Eileen, Enhanced selectivity
502 of carbonaceous products from electrochemical reduction of CO₂ in aqueous media, *Journal*
503 *of CO₂ Utilization*, 30 (2019) 214-221.

504 [23] Y. Peng, T. Wu, L. Sun, J.M.V. Nsanzimana, A.C. Fisher, X. Wang, Selective
505 Electrochemical Reduction of CO₂ to Ethylene on Nanopores-Modified Copper Electrodes in
506 Aqueous Solution, *ACS Appl Mater Interfaces*, 9 (2017) 32782-32789.

507 [24] Y. Fu, Y. Li, X. Zhang, Y. Liu, J. Qiao, J. Zhang, D.P. Wilkinson, Novel hierarchical SnO
508 2 microsphere catalyst coated on gas diffusion electrode for enhancing energy efficiency of CO
509 2 reduction to formate fuel, *Applied Energy*, 175 (2016) 536-544.

510 [25] N. Nilius, H. Fedderwitz, B. Gross, C. Noguera, J. Goniakowski, Incorrect DFT-GGA
511 predictions of the stability of non-stoichiometric/polar dielectric surfaces: the case of
512 Cu₂O(111), *Phys Chem Chem Phys*, 18 (2016) 6729-6733.

513 [26] G.H. Jeong, Y.C. Tan, J.T. Song, G.-Y. Lee, H.J. Lee, J. Lim, H.Y. Jeong, S. Won, J. Oh,
514 S.O. Kim, Synthetic multiscale design of nanostructured Ni single atom catalyst for superior
515 CO₂ electroreduction, *Chemical Engineering Journal*, 426 (2021) 131063.

516 [27] W. Zhang, Y. Hu, L. Ma, G. Zhu, Y. Wang, X. Xue, R. Chen, S. Yang, Z. Jin, Progress
517 and perspective of electrocatalytic CO₂ reduction for renewable carbonaceous fuels and
518 chemicals, *Advanced Science*, 5 (2018) 1700275.

519 [28] J. Rosen, G.S. Hutchings, Q. Lu, S. Rivera, Y. Zhou, D.G. Vlachos, F. Jiao, Mechanistic
520 insights into the electrochemical reduction of CO₂ to CO on nanostructured Ag surfaces, *Acc*
521 *Catalysis*, 5 (2015) 4293-4299.

522 [29] J. Wu, Y. Huang, W. Ye, Y. Li, CO₂ reduction: from the electrochemical to photochemical
523 approach, *Advanced Science*, 4 (2017) 1700194.

524 [30] H. Mistry, A.S. Varela, C.S. Bonifacio, I. Zegkinoglou, I. Sinev, Y.-W. Choi, K.
525 Kisslinger, E.A. Stach, J.C. Yang, P. Strasser, Highly selective plasma-activated copper
526 catalysts for carbon dioxide reduction to ethylene, *Nature communications*, 7 (2016) 1-9.

527 [31] P. Yang, Z.J. Zhao, X. Chang, R. Mu, S. Zha, G. Zhang, J. Gong, The functionality of
528 surface hydroxy groups on the selectivity and activity of carbon dioxide reduction over cuprous
529 oxide in aqueous solutions, *Angewandte Chemie*, 130 (2018) 7850-7854.

530 [32] H. Rabiee, L. Ge, X. Zhang, S. Hu, M. Li, S. Smart, Z. Zhu, Z. Yuan, Shape-tuned
531 electrodeposition of bismuth-based nanosheets on flow-through hollow fiber gas diffusion
532 electrode for high-efficiency CO₂ reduction to formate, *Applied Catalysis B: Environmental*,
533 286 (2021) 119945.

534 [33] W. Zhu, S. Kattel, F. Jiao, J.G. Chen, Shape-controlled CO₂ electrochemical reduction on
535 nanosized Pd hydride cubes and octahedra, *Advanced Energy Materials*, 9 (2019) 1802840.

536 [34] C.-T. Dinh, T. Burdyny, M.G. Kibria, A. Seifitokaldani, C.M. Gabardo, F.P.G. De Arquer,
537 A. Kiani, J.P. Edwards, P. De Luna, O.S. Bushuyev, CO₂ electroreduction to ethylene via
538 hydroxide-mediated copper catalysis at an abrupt interface, *Science*, 360 (2018) 783-787.

539 [35] F.P.G. De Arquer, C.-T. Dinh, A. Ozden, J. Wicks, C. McCallum, A.R. Kirmani, D.-H.
540 Nam, C. Gabardo, A. Seifitokaldani, X. Wang, CO₂ electrolysis to multicarbon products at
541 activities greater than 1 A cm⁻², *Science*, 367 (2020) 661-666.

542 [36] Y. Wang, H. Lei, H. Xiang, Y. Fu, C. Xu, Y. Jiang, B.B. Xu, E.H. Yu, C. Gao, T.X. Liu,
543 Porous Bilayer Electrode Guided Gas Diffusion for Enhanced CO₂ Electrochemical Reduction,
544 *Advanced Energy and Sustainability Research*, (2021) 2100083.

545 [37] H. Rabiee, X. Zhang, L. Ge, S. Hu, M. Li, S. Smart, Z. Zhu, Z. Yuan, Tuning the product
546 selectivity of the Cu hollow fiber gas diffusion electrode for efficient CO₂ reduction to formate
547 by controlled surface Sn electrodeposition, *ACS applied materials & interfaces*, 12 (2020)
548 21670-21681.

549 [38] Z. Yang, D. Li, L. Xing, H. Xiang, J. Xuan, S. Cheng, E.H. Yu, A. Yang, Modeling and
550 Upscaling Analysis of Gas Diffusion Electrode-Based Electrochemical Carbon Dioxide
551 Reduction Systems, *ACS Sustainable Chemistry & Engineering*, 9 (2020) 351-361.

552 [39] J. Li, Z. Mei, L. Liu, H. Liang, A. Azarov, A. Kuznetsov, Y. Liu, A. Ji, Q. Meng, X. Du,
553 Probing defects in nitrogen-doped Cu₂O, *Scientific reports*, 4 (2014) 1-6.

554 [40] Z.-Z. Niu, F.-Y. Gao, X.-L. Zhang, P.-P. Yang, R. Liu, L.-P. Chi, Z.-Z. Wu, S. Qin, X.
555 Yu, M.-R. Gao, Hierarchical Copper with Inherent Hydrophobicity Mitigates Electrode
556 Flooding for High-Rate CO₂ Electroreduction to Multicarbon Products, *Journal of the*
557 *American Chemical Society*, (2021).

558 [41] M.B. Ross, P. De Luna, Y. Li, C.-T. Dinh, D. Kim, P. Yang, E.H. Sargent, Designing
559 materials for electrochemical carbon dioxide recycling, *Nature Catalysis*, 2 (2019) 648-658.

560 [42] J. Park, H. Oh, T. Ha, Y.I. Lee, K. Min, A review of the gas diffusion layer in proton
561 exchange membrane fuel cells: durability and degradation, *Applied Energy*, 155 (2015) 866-
562 880.

563